



Contents lists available at ScienceDirect

Arabian Journal of Chemistry

journal homepage: www.ksu.edu.sa

Original article

Smartphone-enabled mesoporous silica nanotube chemosensors for quick and selective mercury detection in water and cosmetics

Albandary Almahri^a, Nashwa M. El-Metwaly^{b,c,*}^a Department of Chemistry, College of Science and Humanities in Al-Kharj, Prince Sattam Bin Abdulaziz University, Al-Kharj 11942, Saudi Arabia^b Department of Chemistry, Faculty of Science, Umm Al Qura University, Makkah 24230, Saudi Arabia^c Department of Chemistry, Faculty of Science, Mansoura University, Mansoura, Egypt

ARTICLE INFO

Keywords:

Mesoporous silica nanotube
Chemosensors
Mercury detection in water
Cosmetics

ABSTRACT

The pervasive presence of mercury in water and cosmetics poses significant health risks, necessitating the development of a method for the in-situ monitoring and extraction of mercury ions. This study introduces a novel approach utilizing Mesoporous Silica Nanotubes (MSNTs) with a unique worm-like structure, providing an expansive surface area ideal for the adsorption of a Hg²⁺ ion chromophore, N,N,N',N'-Tetramethyl-4,4'-diaminobenzophenone. This configuration enables rapid and visible detection of toxic mercury, with a color transition from yellow to green that is easily discernible by the naked eye. The sensitivity of the Mercury nano-sensor (MNS) is remarkably high, with a detection limit of 1.9×10^{-8} M as determined by digital image analysis, and 4.9×10^{-8} M via spectrophotometric methods—both well below the WHO guidelines for drinking water. The MNS's low detection threshold, coupled with its reusability after simple regeneration, positions it as an effective tool for preliminary water testing. The findings suggest that the MNS, requiring only 10 mg for measurements, offers a promising solution for the real-time visualization of mercury ions, enhancing safety measures in water and cosmetic products.

1. Introduction

Mercury, recognized as a formidable contaminant within ecosystems, is linked to numerous health conditions, including the notorious Minamata disease. Its inability to degrade within biological systems or food chains presents a profound risk to both public health and environmental stability (Zahir et al., 2005; Hylander and Goodsite, 2006; Zheng et al., 2007). Furthermore, mercury's presence can inflict harm upon the endocrine and nervous systems, as well as the brain and kidneys (Clarkson et al., 2003; Wang et al., 2010). Mercury's primary form is the water-soluble inorganic mercurous ion (Hg²⁺). Notable sources of mercury include cement kilns, power stations, thermometers, mercury vapor lamps, chlor-alkali plants, gold extraction processes, and barometers (Natale et al., 2006; Grandjean et al., 1998; Harada, 1995). Mercury's correspondence for thiol groups in proteins and enzymes disrupts cellular functions in humans. According to U.S. EPA standards, the maximum permissible mercury concentration is 2 ppb in water (Mercury Update, 2001). Products such as skin-whitening creams, antiseptic soaps, and eye cosmetics often contain high mercury levels. This metal

can be absorbed through the skin, inhaled, or ingested, leading to accumulation within the body. Methylmercury, a particularly toxic variant, can be absorbed through skin contact with cosmetics or through the consumption of foods like fish. Notably, mercury accumulation in expectant mothers is associated with neurodevelopmental impairments in their offspring (Bose-O'Reilly et al., 2010). Symptoms of mercury exposure include psychological disturbances, skin pigmentation changes, rashes, and diminished resistance to skin infections (El-Sewify et al., 2022). While some products fail to disclose their mercury content, the exposure risk extends beyond individual users to their immediate family members. Cosmetic products can have mercury concentrations ranging from 700 to 30,000 ppm, while the acceptable limit in drinking water is only 2 ppb.

Reliable mercury quantification often employs atomic absorption and mass spectrometry techniques. Nevertheless, these methods come with high costs and the necessity for centralized laboratories. Recent advancements have seen the creation of portable X-ray fluorescence devices, which offer quick mercury assessments in various products, yet they remain financially prohibitive (Brent et al., 2017). Recent years

Peer review under responsibility of King Saud University.

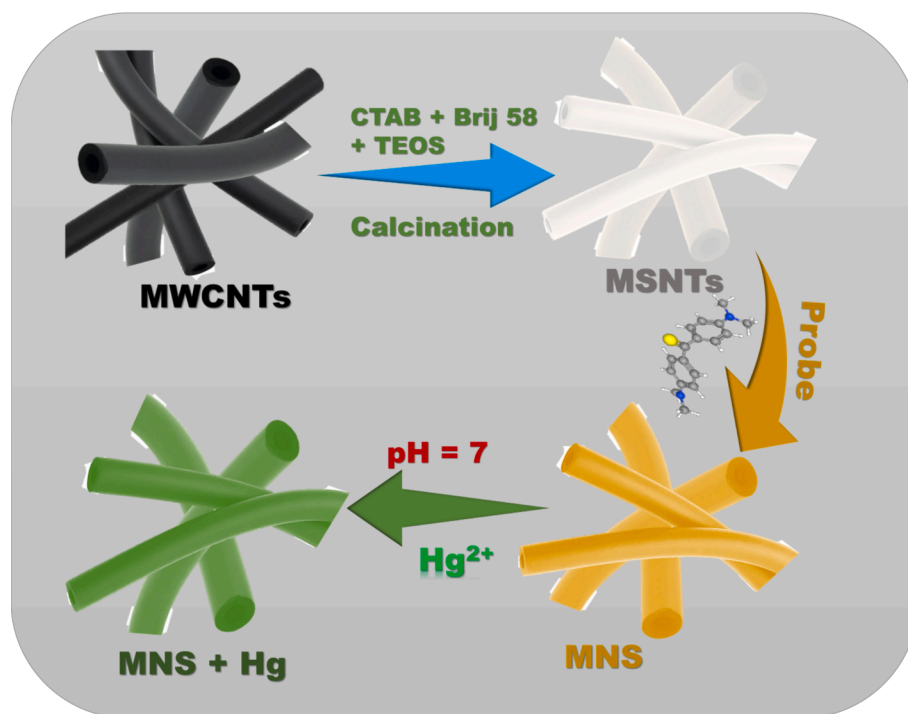
* Corresponding author.

E-mail addresses: a.almahri@psau.edu.sa (A. Almahri), n_elmetwaly00@yahoo.com, nmmohamed@uqu.edu.sa (N.M. El-Metwaly).<https://doi.org/10.1016/j.arabjc.2024.105984>

Received 29 April 2024; Accepted 31 August 2024

Available online 2 September 2024

1878-5352/© 2024 The Author(s). Published by Elsevier B.V. on behalf of King Saud University. This is an open access article under the CC BY-NC-ND license (<http://creativecommons.org/licenses/by-nc-nd/4.0/>).



Scheme 1. Schematic representation of MSNTs formation, probe immobilization on the MSNTs structure, and the optical signalling response of the MNS towards Hg^{2+} ions.

have witnessed the emergence of analytical methods for mercury ion detection, such as electrochemical sensing (Fu et al., 2011; Leermakers et al., 2005), atomic absorption spectrometry (AAS) (Gao et al., 2010), and inductively coupled plasma mass spectrometry (ICP-MS) (Moreno et al., 2010). A shared limitation of these techniques is their reliance on costly, complex equipment. On the flip side, molecular optical sensing allows for the monitoring of a specific analyte by connecting an optical signal transducer to a selective recognition element (Chen et al., 2015). Compared to traditional methods, spectrophotometry offers several advantages, including straightforward procedures, swift operation, heightened sensitivity, ease of use, affordability of the apparatus, and the capacity for concurrent detection (You et al., 2015; Khalil et al., 2016).

Chemo-sensors have an advantage because they can convert ion concentration into signals that can be easily understood by standard devices or even by people without specialized training. A chromogenic sensor is what we call it when the signal causes a visible color change, and this is especially helpful. Essentially, a sensor is an integrated analytical device that converts the concentration of a chemical entity into a readable signal for either an observer or an instrument (McGrath and Scanail, 2013; Radwan et al., 2020). Chemo-sensors based on mesoporous silica have garnered attention for their superior efficacy in detecting small organic compounds (Shahat et al., 2015; Radwan et al., 2022; Shahat et al., 2020; Radwan et al., 2020; Kamel et al., 2020). However, the literature is scant on the development of solid-state chemo-sensors tailored for Hg^{2+} ion detection (El-Sewify et al., 2023). Therefore, the creation of cost-effective, user-friendly, rapid-response, and highly selective chemo-sensors for mercury ion analysis, particularly those enabling straightforward and visual detection, remains an enticing yet formidable task.

A plethora of studies have delved into the intricate interplay between silica entities and surfactants to synthesize specific mesoporous silicas (Hudson et al., 2008; Hassan et al., 2020; Hasan et al., 2014; Hasan, 2014; Hasan and Znad, 2015; Khaleque et al., 2015). The combination of inorganic and organic elements results in the self-organization of surfactant-silica nanocomposites. The physical attributes and structures

of these materials are largely influenced by the dynamics of sol-gel processes, which are governed by factors such as the pH level, water content, and temperature of the reaction milieu (Pan et al., 2018; El-Sewify et al., 2022; Ioannou-Ttofa et al., 2019; Du et al., 2021; Zhu et al., 2023; Zhang et al., 2022; El-Sewify et al., 2024; Khalil et al., 2024; Basha et al., 2024; Mohamed et al., 2024; Hosni et al., 2024; Rizk et al., 2024; Al-Hazmi et al., 2022; Awual et al., 2017; Abd El-Fattah et al., 2024; Ali et al., 2021; Shahat et al., 2022; Abd El-Fattah et al., 2024; Abd El-Fattah et al., 2024), as well as the thermodynamic properties of the surfactant-silica system (Pulicharla et al., 2017). By meticulously managing the rate of silica polymerization and the self-assembly process, one can customize the mesostructures, morphologies, and dimensions of the mesoporous silicas (Brühwiler, 2010). The burgeoning attention in mesoporous silica (MSNs) stems from their uniform mesopores, straightforward surface modification, and notable biocompatibility, making them ideal for biomedical applications. Their expansive surface area and voluminous pore spaces lay the groundwork for devising a versatile theranostic platform (Wang et al., 2016). MSNs are characterized by three distinct functional zones: the nanochannels/pores, the nanoparticle's external surface, and the silica matrix. These nanoparticles are further distinguished by their simple surface modification, biological compatibility in living organisms, and efficient cellular internalization (Chung et al., 2007; Mazrouaa et al., 2019).

This study introduces innovative solid chemo-sensors created by anchoring N,N,N,N'-Tetramethyl-4,4'-diaminobenzophenone onto the mesoporous structure of silica nanotubes (MSNTs). These sensors serve as chromogenic detectors, offering a highly selective, swift, and visual method for identifying Hg^{2+} ions. The resulting color change is discernible to the naked eye and can be monitored using commonplace devices like smartphones or through spectrophotometric techniques. Digital image-based colorimetry (DICA) is a novel approach that leverages these technologies for precise quantitative analysis in the field of analytical chemistry. Sample images are captured with a smartphone camera and an accompanying app, with RGB values computed on the spot. These RGB metrics are then employed to measure the concentrations of target analytes. The time required to achieve a consistent signal

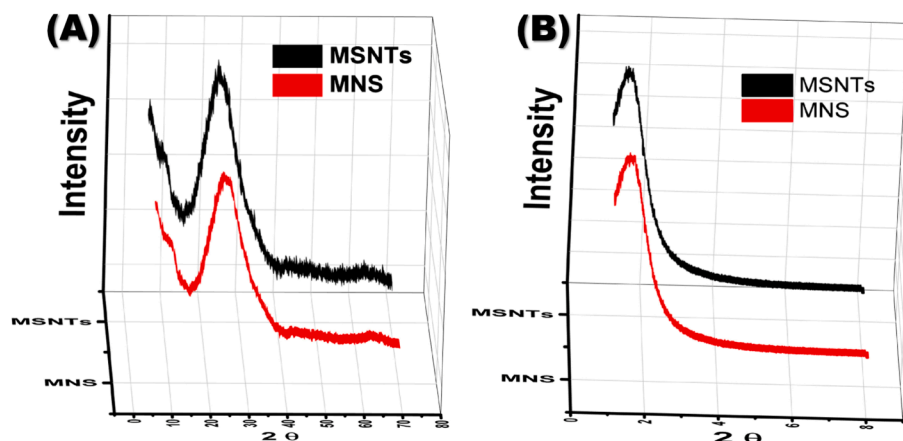


Fig. 1. (A) WAXRD and (B) LAXRD diffraction patterns of the MSNTs and MNS.

is remarkably brief (under 20 s). The merits of this technique include its simplicity, speed, cost-effectiveness, and accessibility to non-specialists. Digital image analysis has determined the detection threshold for Hg^{2+} ions to be 4.9×10^{-8} M, while the spectrophotometric approach has a limit of 1.9×10^{-8} M. MSNs have proven effective in detecting and extracting ultra-low concentrations of Hg^{2+} ions from water and skin-lightening cosmetic products.

2. Experimental work

2.1. Materials and instruments

Detailed descriptions of all materials and instruments used in this work are provided in the [supporting information file](#).

2.2. Preparation of mesoporous silica nanotubes (MSNTs)

In preparing innovative mesoporous silica nanotubes, 0.25 gm of multiwall carbon nanotubes were distributed in 100 mL of Milli-Q water. Then, it was subjected to sonication for 30 min to ensure uniform suspension. Subsequently, 2 gm of cetyltrimethylammonium bromide was added, and the solution was stirred continuously for over 2 h. Following this, 1.0 gm of Brij 58, pre-dissolved in 4 mL of acetone, was added to the mixture, which was then stirred for an additional hour. To form the coating silica, 2.5 mL of TEOS was incorporated. The mixture was then stirred vigorously for another hour, after which 1.5 mL of NH_4OH (25 wt%) was added. Vigorous stirring was applied to the reaction, which was allowed to proceed for 24 h at room temperature in a sealed container. The MSNTs@MWCNTs (shell@core) composite was gathered via centrifugation. The MSNTs@MWCNTs were collected and purified using isopropanol. They were then dried at 80°C for 24 h. After that, they underwent calcination for 6 h at 500°C . Finally, they were heated for an additional 8 h at the same temperature (Scheme 1).

2.3. Design of mercury nano-sensor (MNS)

The MSNs were synthesized through a straightforward immobilization technique. A combination of the organic chromophore N,N,N,N'-Tetramethyl-4,4'-diaminobenzophenone (50 mg) with MSNTs (1 g) was agitated in ethanol for 4 h. After the stirring, the blend underwent filtration and was left to dry. The platform's hue visibly changed, signaling the successful bonding of the organic chromophore to the nanotube's surface. To ensure complete pore occupancy within the carrier, this process was executed multiple times. Following these steps, the resultant MSNs were purified using deionized water and desiccated at 50°C throughout the night.

2.4. Analysis of the ultra-trace Hg^{2+}

To prepare a Hg^{2+} stock solution with a concentration of 200 ppm, we added 0.0271 g of HgCl_2 to a 100.0 mL volumetric flask. We also added a few droplets of 3.0 M hydrochloric acid to prevent the precipitation of $\text{Hg}(\text{OH})_2$. Then, we diluted the mixture with deionized water. The resulting solution was transferred to a 1 cm quartz cuvette, and a measured quantity of the Hg^{2+} solution was added. We promptly acquired UV-vis spectroscopic profiles without any agitation. For liquid/solid sensing assays, we used a phosphate-buffered medium to maintain the Hg^{2+} ion concentrations at a neutral pH of 7. In addition, 10 mg of MNS chemo-sensors were added to both the blank solution and the solution containing Hg^{2+} . Each solution had a volume of 20 mL and was agitated at 25°C . The mixtures were sonicated for 60 s and then analyzed using a UV-vis spectrophotometer. The colorimetric assessment of Hg^{2+} ions using MNS nanotubes was studied across a wide pH range. The sensing parameters included a dosage of 10 mg of MNS, a Hg^{2+} concentration of 2 ppm, and a total volume of 10 mL. The absorbance spectra were recorded after equilibrium was reached. In order to quantify mercury in cosmetic products, the samples were treated with nitric acid to extract Hg^{2+} ions from any methylmercury compounds that could be present.

3. Results and discussion

CTAB, a surfactant commonly utilized for the dispersion of nanoparticles and their transition from organic to aqueous phases (Yang et al., 2011), serves as a foundational element for the mesoporous silica coating of nanoparticles. Additionally, CTAB is frequently employed as a template in the synthesis of mesoporous silica (Zhao and Wan, 2007), underscoring the importance of establishing a straightforward, universal protocol for mesoporous silica coatings within the CTAB framework.

The MSNTs, characterized by their biocompatibility, porous structure, surface functionality, and hydrophilic design, have garnered significant interest due to their one-dimensional hollow inorganic architecture (Gao et al., 2011; Yang et al., 2011; Abou-Melha et al., 2021). The fabrication process (Scheme 1) ensured precise control over the dimensions of these novel MSNTs. The process started by suspending MWCNTs in deionized water, then forming a silica shell to make MSNTs@MWCNTs. The complete removal of MWCNTs from the composite was verified through XRD analysis, which included both low- and wide-angle diffraction patterns. The WAXRD of the MSNTs and MNS exhibited a characteristic broad peak spanning the $18\text{--}38^\circ$ range, indicating the amorphous nature of the nanotube walls, as depicted in Fig. 1A. Additionally, the LAXRD patterns revealed a shoulder peak at $2\theta \approx 1.37^\circ$, confirming the presence of an ordered mesostructure, as illustrated in Fig. 1B. The LAXRD and WAXRD profiles showed that the

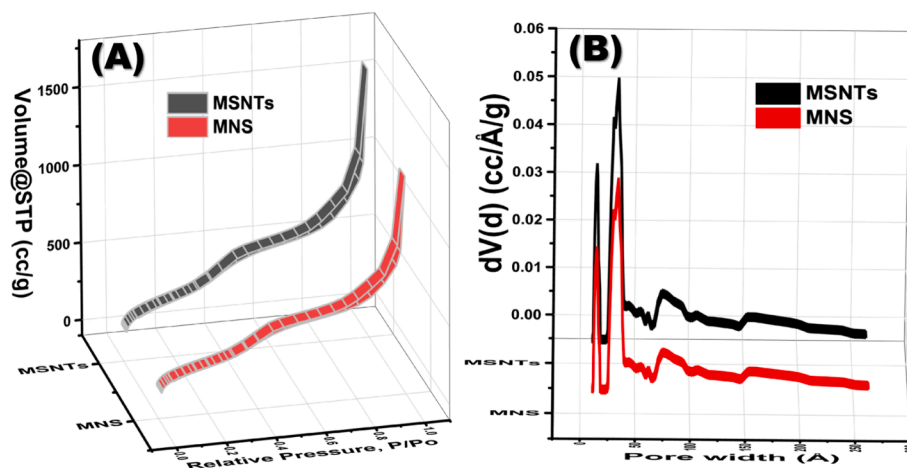


Fig. 2. Nitrogen adsorption–desorption analysis of the MSNTs and MNS and pore size distributions of the MSNTs and MNS (B).

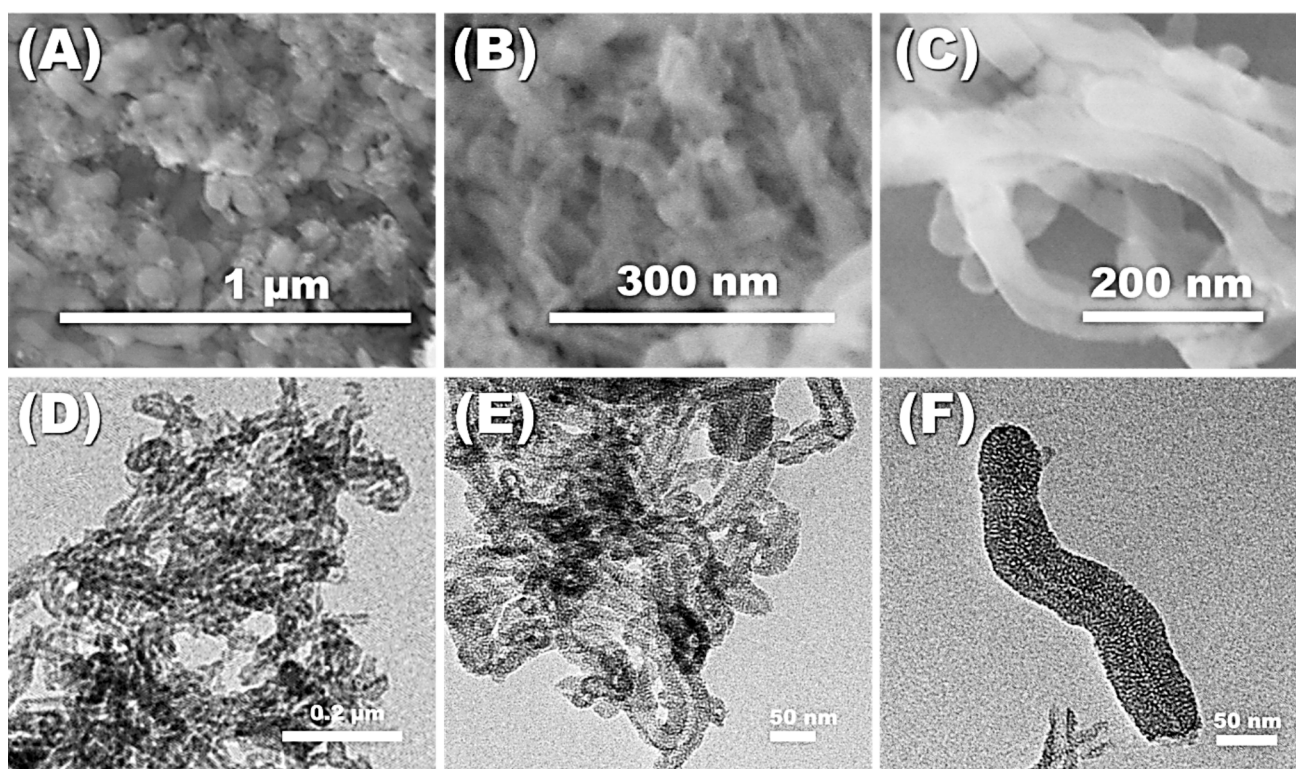


Fig. 3. Representative FESEM images of (A) the MSNTs, (B) the MNS chemosensor, and (C) the MNS chemosensor after many times of reusability, the TEM images of (D) the MSNTs, (E) the MNS chemosensor, and (F) the MNS chemosensor after many times of reusability.

sensor (MNS) and its precursor, the MSNTs carrier, have similar structures. This suggests that the immobilization process maintains the integrity and order of the MSNTs' mesostructure.

The MSNTs and MNS show Type IV classification in their nitrogen adsorption–desorption isotherms, as depicted in Fig. 2. These isotherms display dual hysteresis loops within the MSNTs' isotherm, indicating the presence of mesoporous structures enabled by capillary condensation. The mesopores within the SiO₂ layer produce a minor hysteresis loop in the P/P₀ range of 0.3 to 0.5 after CTAB extraction. Conversely, the pronounced hysteresis loop at P/P₀ values exceeding 0.8 is ascribed to the intrinsic mesopores of the MSNTs themselves (Vila et al., 2009). Post-immobilization of the organic chromophore, a reduction in the MSNTs' surface area is evident from the N₂ isotherms (Fig. 2A). The Brunauer-Emmett-Teller (BET) surface area of the MSNTs is quantified

at 1120 m²/g, surpassing that of the MNS, which is 922 m²/g. Similarly, the pore volume of the MSNTs, measured at 1.56 cm³/g, exceeds the MNS's 1.33 cm³/g (Fig. 2B). The preservation of chromophores both on the exterior and interior of the nanotubes accounts for the diminished pore volumes and surface areas observed in the MNS. These findings elucidate the systematic process of infilling and ornamenting the microporous voids within the MSNTs with organic receptors.

The morphological characterization of MSNTs was conducted using SEM and TEM techniques, with the findings illustrated in Fig. 3. Initially, the pristine MWCNTs exhibited an average diameter ranging from 15–30 nm. Post-coating with mesoporous SiO₂, a notable increase in diameter to approximately 55–85 nm was observed, indicative of a 40–50 nm thick SiO₂ mesoporous layer enveloping the MWCNTs. TEM analysis corroborated the uniform coating of the mesoporous SiO₂ layer

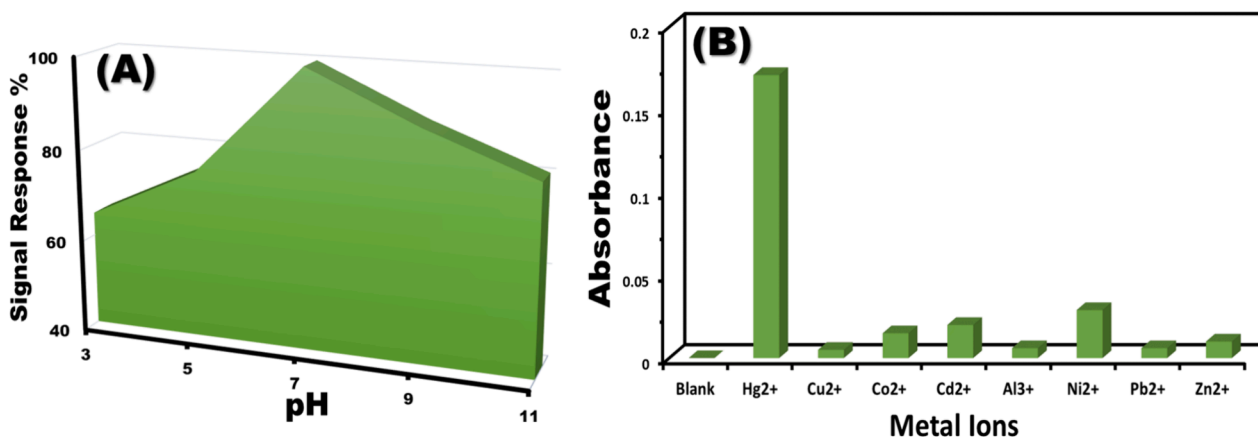


Fig. 4. (A) pH-dependent response of MNS optical chemosensors to 1 ppm Hg²⁺ ions. (B) Interference studies: Effect of common interfering cations on the absorbance spectra of MNS chemosensors.

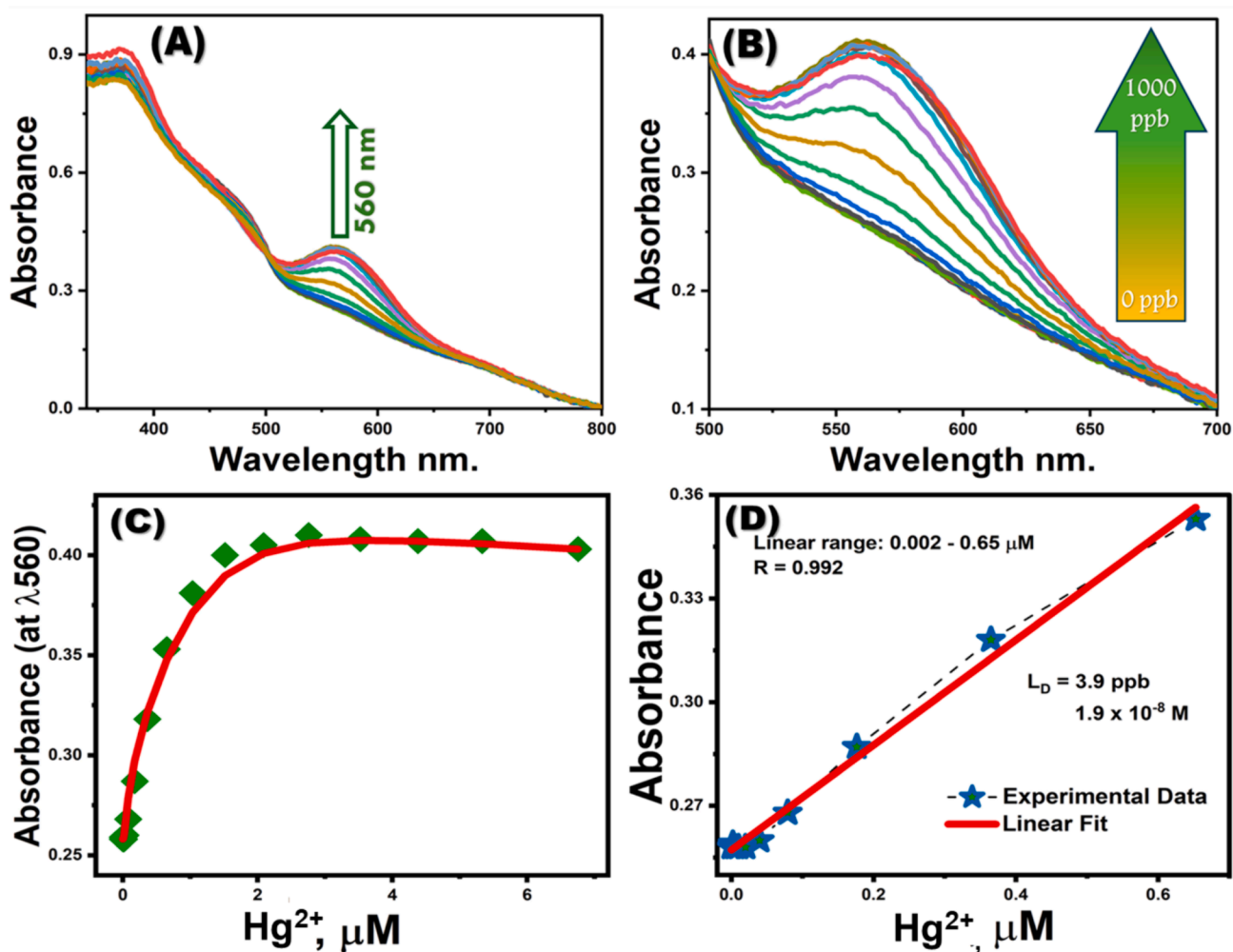


Fig. 5. (A, B) Absorption spectra of MNS optical chemosensors titrated with Hg²⁺ ions. (C) Calibration curves for MNS optical chemosensors, measured at λ560nm. (D) Linear-fit line within the linear concentration range of the calibration plots for MNS optical chemosensors at λ560nm with varying Hg²⁺ concentrations.

across all samples, with minimal free SiO₂ particles detected. Intriguingly, most of the pores were aligned perpendicular to the MWCNTs' surface, a feature that is anticipated to enhance mass transfer across the silica coating's inner and outer surfaces, thereby rendering this structure advantageous for nanocarrier applications (Ding et al., 2009).

SEM imagery (Fig. 3A-C) revealed the engineered morphology of the

nanotube structures, which were dispersed and interconnected randomly, forming the MSNTs' cavities. These carriers were synthesized through reproducible methods that ensured control over the structural morphology. The emergence of a worm-like structure is attributed to the Si-O-Si interactions, leading to the spontaneous assembly and clustering of silicon dioxide around the MWCNTs. The dispersion of the carrier in

Table 1
Comparative Analysis of Spectrophotometer and Digital Image-Based Colorimetric Techniques.

Parameters	Spectrophotometric method	(DICA) method
L_D (M)	1.9×10^{-8}	4.9×10^{-8}
D_R (μ M)	0.002 to 0.65	0.024 to 0.5
L_Q (M)	6.5×10^{-8}	1.3×10^{-7}
R^2	0.992	0.986

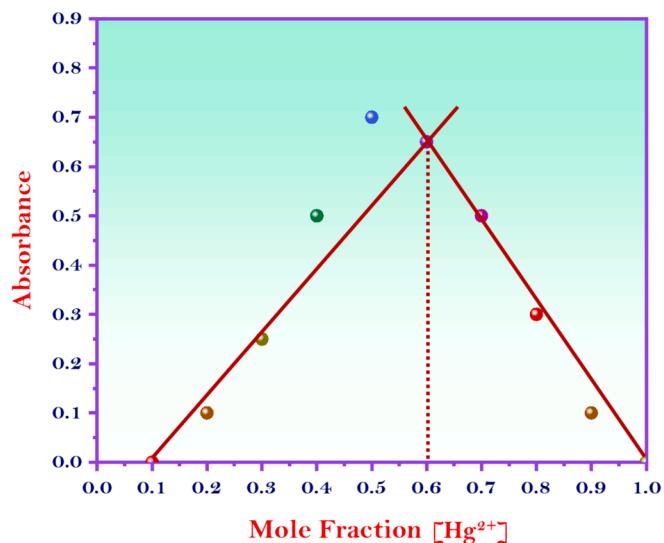


Fig. 6. Job's plot analysis for the interaction between the MNS and the Hg^{2+} ions.

the solution regulated the self-assembly of MSNTs and the formation of significant openings. TEM images (Fig. 3D–F) displayed the MSNTs arranged asymmetrically to create significant openings. The findings

demonstrate that cylindrical MSNTs, with diameters around 65 nm, were randomly clustered and layered around the cavities, encapsulating the highly sensitive receptors. A uniform coating of dense, thin organic receptor layers was applied to the MSNTs' cavities, culminating in the MNS. The direct immobilization of organic chromophore onto the silica nanotubes facilitated ongoing monitoring, rapid detection (within seconds), and the capture of Hg^{2+} contaminants in both water and cosmetic products. The chromophores were incorporated without affecting the structural morphology of the MSNTs. This was confirmed by the FESEM image (Fig. 3 B) and the TEM image (Fig. 3 E). In addition, the FESEM image (Fig. 3 C) and the TEM image (Fig. 3 C) confirm the stability of the sensor even after reusability many times.

3.1. Quantitative determination of mercury(II) ions using UV–Vis spectrophotometry

A major challenge in chemical sensors is creating optical chemosensors that are highly stable. The long-lasting stability of the carefully crafted optical chemosensors is demonstrated by minor fluctuations in sensor performance over time, especially during storage. Spectral analyses of these sensors have consistently yielded uniform results, affirming the absence of sensitivity degradation post-storage in an opaque container.

The optimal sensing parameters greatly affect the fidelity and intensity of color distribution, which is crucial for detecting ultratrace levels of mercury ions. To ascertain the efficacy of MNS optical chemosensors, various factors were scrutinized, including the limitations of Hg^{2+} ion detection, pH levels, response duration, and the quantity of chemosensors employed (measured in milligrams). The absorbance spectra in Fig. 4A were carefully examined to find the optimal pH for detecting Hg^{2+} ions. A gamut of standard Hg^{2+} ion solutions was fine-tuned with diverse buffer solutions. At a neutral pH of 7, a pronounced absorbance spectrum was observed, designating it as the optimal condition for Hg^{2+} ion sensing.

The test samples were exposed to standard solutions containing common interfering cations to investigate the selectivity of MNS

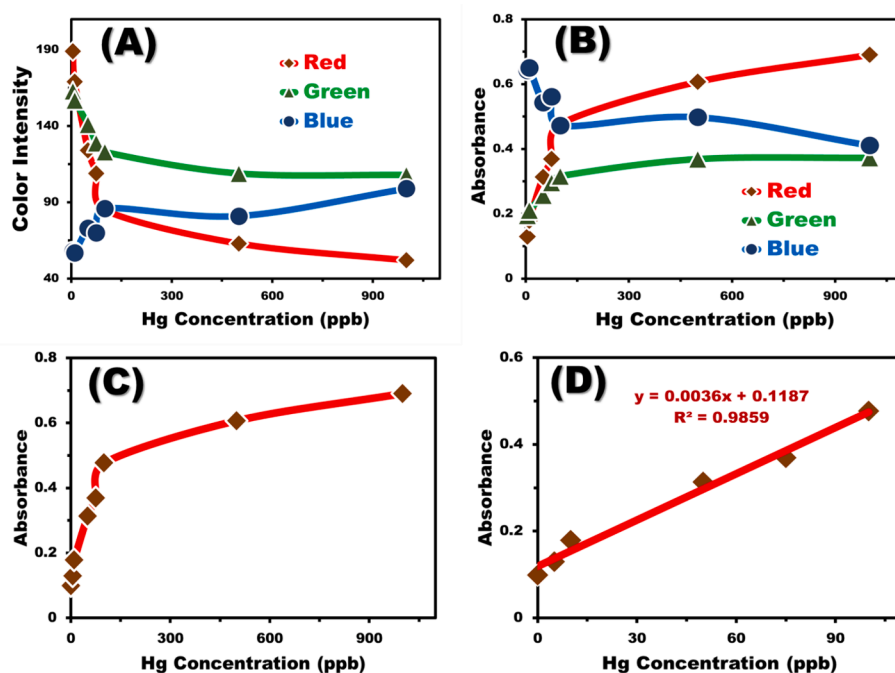


Fig. 7. (A) Correlation between Hg^{2+} ion concentrations and RGB intensities derived from digital images analyzed using the Histogram tool. (B) Relationship between Hg^{2+} ion concentrations and calculated RGB absorbances for mobile camera images. (C) Correlation between Hg^{2+} ion concentrations and the calculated absorbance of red color, demonstrating an increase in red color absorbance with rising Hg^{2+} ion concentrations. (D) Linear correlation between red color absorbance and Hg^{2+} ion concentration. (For interpretation of the references to color in this figure legend, the reader is referred to the web version of this article.)

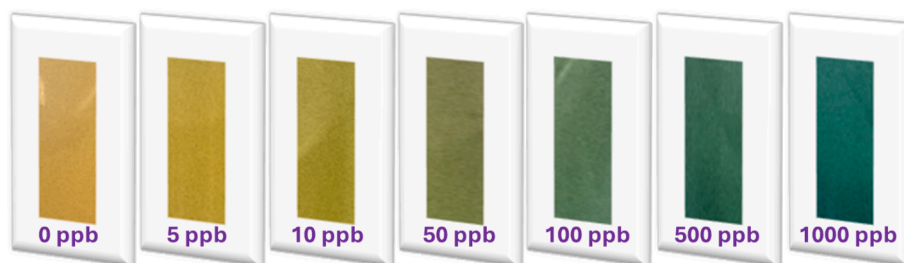


Fig. 8. Captured input pics for the DICA, showcasing the complexation between Hg^{2+} and the MNS probe across various concentrations.

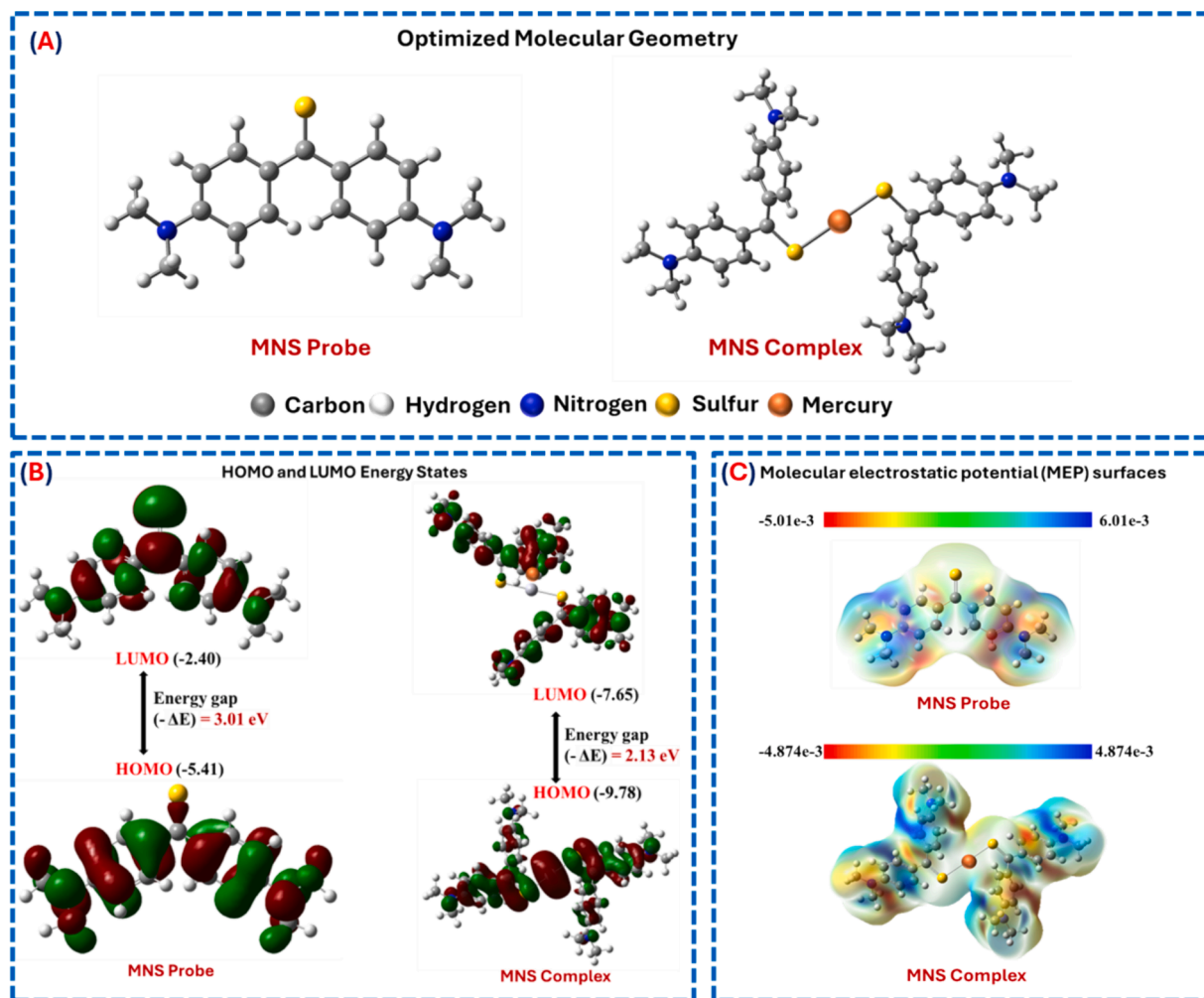


Fig. 9. (A) Optimized molecular geometry of the MNS probe and MNS-Hg(II) complex. (B) Frontier molecular orbital (FMO) analysis of the MNS probe and MNS-Hg(II) complex. (C) Molecular electrostatic potential (MESP) mapping of the MNS probe and MNS-Hg(II) complexation.

chemosensors for Hg^{2+} detection. The spectrophotometric measurements were carried out at a wavelength of $\lambda = 560$ nm, following the optimal conditions (pH 7, ambient temperature, 10 mL sample volume, and 10 mg sensor dosage). Fig. 4B illustrates that the introduction of interfering ions did not significantly alter the absorption spectra. However, the addition of Hg^{2+} ions resulted in the emergence of a new absorbance peak at $\lambda = 560$ nm. The absorbance of common ions was documented, revealing a marked enhancement in the absorption spectra upon Hg^{2+} ion interaction. The established tolerance levels for various interfering ions are as follows: Cu^{2+} (20 ppm), Zn^{2+} (100 ppm), Pb^{2+} (100 ppm), Co^{2+} (100 ppm), Al^{3+} (100 ppm), Ni^{2+} (100 ppm), and Cd^{2+} (100 ppm). These results affirm the MNS chemosensors' exceptional specificity for Hg^{2+} ions.

Under the designated optimal sensing conditions, the absorbance of the MNS chemosensor was meticulously examined (refer to Fig. 5A, B). At the peak wavelength (λ_{max}) of 560 nm, a notable intensification in the MNS absorption spectra was observed in tandem with the escalating concentrations of Hg^{2+} ions. This amplification in absorbance intensity is ascribed to the charge transfer occurring during the formation of the complex. The calibration curve for the MNS demonstrated a direct linear relationship with the Hg^{2+} ion concentrations at lower levels, as depicted in Fig. 5C. This linear correlation (illustrated in Fig. 5D) facilitates the tracking of Hg^{2+} ions in ultra-trace quantities, within the highly sensitive detection range of 0.002 – 0.65 μM . The color transition upon the creation of the MNS- Hg^{2+} complex was discernible to the naked eye, negating the need for intricate methodologies. The calculated

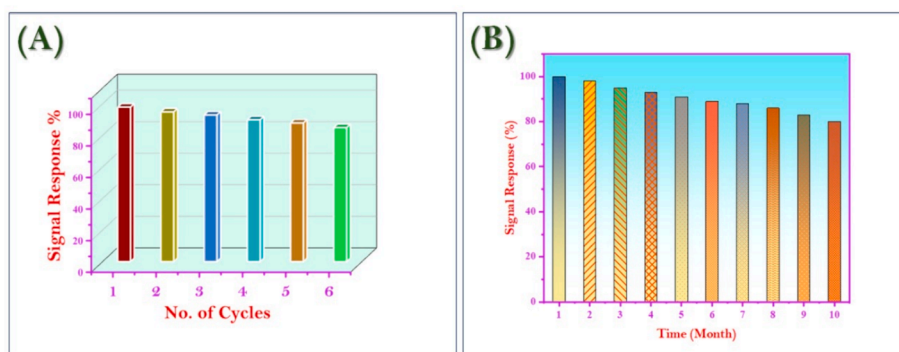


Fig. 10. (A) Reuse study of MNS material (B) Long-term performance and stability study for the MNS material.

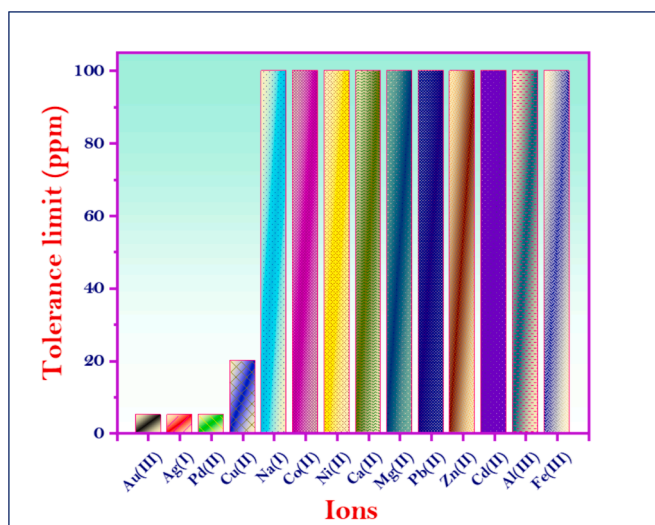


Fig. 11. Effect of interfering ions on the detection of Hg^{2+} ions using MNS optical chemosensors.

limit of detection (LOD) for Hg^{2+} ions operating the MNS chemosensors was determined to be $1.9 \times 10^{-8}\text{M}$, comfortably below the permissible threshold for water (as outlined in Table 1).

The interaction between Hg^{2+} ions and the MNS material resulted in the formation of $\text{Hg}_2\text{-MNS}$ complexes. This 1:2 stoichiometric ratio between MNS and Hg^{2+} ions was further set through Job's plot analysis (Fig. 6.). The visual manifestation of these complexes is clearly evident in the images presented in Fig. 6.

Limit of detection (L_D), detection range (D_R), Limit of quantitation (L_Q).

3.2. Hg^{2+} ion sensing with digital image-based colorimetry

The histogram tool, pivotal in digital image-based colorimetry

Table 2

Determination of $\text{Hg}(\text{II})$ in water and Cosmetic samples.

Sample	ICP-MS Analysis (ppm)	Amount spiked of $\text{Hg}(\text{II})$ (ppb)	Proposed method					
			Spectrophotometer			DICA		
			Recovery	E%	Error %	Recovery	E%	Error %
Tap Water Sample 1	521 ppm Ca^{2+} , 1056 ppm Mg^{2+} , 1.8 ppm Fe^{2+} , 1.6 ppm Fe^{3+}	20	18.9	94.5	5.5	17.8	89	11
Tap Water Sample 2	619 ppm Ca^{2+} , 305 ppm Mg^{2+} , 1.1 ppm Fe^{2+} , 1.8 ppm Fe^{3+}	50	48.5	97	3	47.9	95.6	4.4
*Cosmetic Sample 1	0.1 ppm (100 ppb)	–	98.2	98.2	0.8	97.4	97.4	2.6

* Cosmetic sample after digestion with nitric acid.

analysis (DICA), scans each pixel within the selected color regions to deduce the mean integer values of Red, Green, and Blue (RGB) intensities. These intensities (IR, IG, and IB) correlate with the concentration of Hg^{2+} ions, as illustrated in Fig. 7A. Notably, the intensities of the green (IG) and red (IR) components diminish as the Hg^{2+} ion concentration increases, while the blue intensity (IB) remains relatively unchanged. The predominance of the red component in the sensor's color response is consistent with the spectrophotometric method, which shows high absorption at 560 nm. By associating the color intensity with the absorbance at each concentration level, a calibration curve can be constructed that mirrors the one obtained from the spectrophotometric method (shown in Fig. 7B and C and Fig. 8). Fig. 7D corroborates that Hg^{2+} ions can be sensitively detected at extremely low concentrations, specifically $4.9 \times 10^{-8}\text{M}$. Table 1 discusses the DICA analytical parameters, highlighting a performance that rivals that of the spectrophotometric method. The analytical parameters gleaned from the use of a mobile camera device substantiate the efficacy of DICA for the rapid sensing of toxic Hg^{2+} ions within seconds. Thus, DICA emerges as a competitive alternative for the quantification of mercury ion concentrations.

3.3. Computational analysis of MNS probe and its interaction with Hg^{2+}

Using density functional theory (DFT) and the Gaussian 09 program (Ambroise et al., 2021; Sarangi et al., 2020; Fouda and Besley, 2018; Besley, 2021), a theoretical analysis was performed to understand the binding mechanism between the MNS probe and Hg^{2+} ions, including energy level assessments. The electronic structure of the MNS probe and [(MNS)₂-Hg(II)] complexes was characterized, focusing on their HOMO and LUMO using different functional basis sets. The optimized geometrical structures of the MNS probe and the MNS-Hg(II) complex are displayed in Fig. 9A.

Furthermore, the binding energy and charge transfer mechanism of the MNS probe and the MNS-Hg(II) complex were assessed using Frontier Molecular Orbital (FMO) analysis, as shown in Fig. 8B. Surprisingly, our research indicates that the MNS probe, which includes ligating groups like (=S), had a more positive interaction with $\text{Hg}(\text{II})$ at a binding

ratio of 2:1 (Marczenko and Balcerzak, 2000). The energy transition differences ($E_{\text{HOMO}}-E_{\text{LUMO}}$) indicate that the MNS probe has an energy band gap value of 3.01 eV, while the MNS-Hg(II) complex has a value of 2.13 eV, as shown in Fig. 9B. The observed decrease in the band gap suggests that the MNS probe has effectively interacted with Hg(II), as indicated by the hyperchromic shift in absorption spectra.

The presence of sulfur atoms in the MNS probe significantly contributed to the stability of the Hg-S bond. Additionally, a MESP 3D mapping of both the MNS probe and the [(MNS)₂-Hg(II)] complex was performed to identify active coordination sites and the electrostatic potential distribution across the molecule, shown in Fig. 9C. Electrophilic, neutral, and nucleophilic potentials were identified through visual inspection, each represented by distinct colors—blue, green, and red, respectively. Regions showing a red stain, which indicates negative potential due to active functional groups (=S and -N-CH₃), improved the chances of strong binding interaction with Hg²⁺ when forming complexes using the MNS probe. Complex formation led to a significant enhancement in negative potential, primarily attributed to the stable coordination of the =S—Hg bond. Thus, the presence of functional groups such as =S in MNS molecules was found to be essential in promoting the formation of charge transfer transition complexes with Hg(II), as demonstrated by MESP analysis.

3.4. Reusability and long-term stability analytical assessment for the MNS

The MNS sensor's performance was evaluated in terms of long-term stability and reusability. To assess reusability, the sensor was subjected to multiple cycles of Hg²⁺ ion detection and regeneration. Following Hg²⁺ ion recognition, the MNS material was regenerated by decomplexing the bound Hg²⁺ ions using 2 mL of 0.05 M thiourea (Fig. 10A). The regenerated MNS exhibited minimal changes in absorbance compared to a blank sample, indicating the absence of probe molecule leaching. The sensor demonstrated excellent reusability, maintaining its sensing efficiency for up to six cycles. Beyond this point, a slight decline in performance was observed, potentially due to minor probe detachment from the MSNT carrier. Fig. 3 C&F confirm the stability of the morphology of the MNS chemosensor even after many times reusability.

To evaluate the sensor's long-term stability, its color and spectral response were monitored over a period of 10 months (Fig. 10B). The results demonstrated the chemical stability of the MNS material toward Hg²⁺ ion detection, indicating its suitability for prolonged use without significant performance degradation.

3.5. Analytical assessment of the presence of competing during Hg²⁺ detection with MNS

To evaluate the MNS's selectivity for Hg²⁺ ions amidst potential interfering species, rigorous selectivity and competitive experiments were conducted. The sensor's performance was assessed under optimized conditions. The tolerance limit, specified as the maximum interfering ion concentration causing less than a five percent error in absorbance measurements, was determined. As comprehensively detailed in Fig. 11, the MNS exhibited exceptional selectivity for Hg²⁺ ions. While the MNS demonstrated high performance for most tested ions, the influence of Au³⁺, Ag⁺, and Pd²⁺ was mitigated through the addition of 1 mL of 2 mM sodium thiosulfate solution as a masking agent. The MNS's consistent detection of Hg²⁺ ions in the existence of significant concentrations of other ions underscores its potential for practical applications in complex matrices.

3.6. Applicability of MNS nanotubes

In the practical application of MNS chemosensors, various water samples and skin-whitening creams were subjected to mercury ion detection. Under the established optimal sensing parameters, the water

samples collected from different locations were spiked with a consistent concentration of Hg²⁺ ions. The water samples underwent a triplicate analysis for mercury ion detection, which was later confirmed by ICP-MS testing. The congruence between the ICP-MS data and our findings underscores the efficacy and competitiveness of the MNS chemosensors in mercury detection, as detailed in Table 2. For the skin-whitening cream samples (containing methylmercury as a source of mercury), a pre-treatment involving digestion of 1 g of sample with 10 mL concentrated nitric acid, followed by filtration then dilute the solution to 100 mL for further analysis. Subsequently, 10 mg of MNS optical chemosensors were introduced to the treated samples under optimal conditions. The data pertaining to these samples, as compiled in Table 2, demonstrate the chemosensors' exceptional selectivity and sensitivity in quantifying Hg²⁺ ion concentrations. This reinforces the potential of MNS chemosensors as a reliable tool for mercury detection in real-world scenarios.

4. Conclusion

The culmination of this research has yielded MNS optical chemosensors that stand out for their water stability and enduring structural integrity, maintaining uniform morphology over extended periods. The MSNTs carriers, functionalized with chromophores, facilitate ease of use in both solution and solid states, enabling spectrophotometric analysis. These chemosensors are adept at detecting Hg²⁺ ions in ultra-trace amounts in aqueous environments and skin-whitening products, boasting a detection threshold a hundredfold more sensitive than chromophore applications alone, and surpassing the sensitivity of several previously reported Hg²⁺ optical sensors. The rapid response time of these sensors, clocking in at under 20 s to reach signal stability, coupled with the visually discernible color shift, enhances their user-friendliness. This color change can be conveniently monitored via smartphones or spectrophotometric methods. The high reversibility and reproducibility of the MNS chemosensors, along with their multiple-use capability, underscore their practicality. At an optimal pH of 7 and a temperature of 25 °C, the MNS chemosensors exhibit unparalleled selectivity for Hg²⁺ ions, making them highly suitable for water quality analysis. The long-term stability of these chemosensors is remarkable, ensuring sustained efficiency over numerous applications. The UV-Vis spectrophotometer has determined a detection limit of 1.9×10^{-8} M for the MNS nanomaterials. Furthermore, the integration of mobile phone cameras and computer software has demonstrated a comparable sensitivity, with a detection limit as low as 4.9×10^{-8} M. The findings from this study confirm the MNS chemosensors' potential for effective monitoring and sequestration of Hg²⁺ ions, positioning them as an asset in environmental and health safety applications.

CRedit authorship contribution statement

Albandary Almahri: Writing – original draft, Software, Resources, Methodology, Funding acquisition, Formal analysis. **Nashwa M. El-Metwaly:** Writing – review & editing, Visualization, Supervision, Project administration, Data curation.

Declaration of competing interest

The authors declare that they have no known competing financial interests or personal relationships that could have appeared to influence the work reported in this paper.

Acknowledgments

The authors extended their appreciations to Princes Sattam bin Abdulaziz University for funding this research work through the project number (PSAU/2024/01/28923).

Appendix A. Supplementary material

Supplementary data to this article can be found online at <https://doi.org/10.1016/j.arabjc.2024.105984>.

References

- Abd El-Fattah, W., Guesmi, A., Ben Hamadi, N., Khalil, M.A., Shahat, A., 2024. A highly sensitive chemosensor based on a metal-organic framework for determining zinc ions in cosmetics creams and wastewater. *Appl. Organomet. Chem.* 38 (5), e7407.
- Abd El-Fattah, W., Guesmi, A., Hamadi, N.B., Subaihi, A., Shahat, A., 2024. Extraction and detection of mercury in electronic waste using efficient modified MOF. *Colloids Surf. A Physicochem. Eng. Asp.* 686, 133256.
- Abd El-Fattah, W., Guesmi, A., Hamadi, N.B., Alayyafi, A.A., Shahat, A., 2024. Novel composite based on cellulose nanomaterial for detection and selective removal of cadmium (II) ions from wastewater. *Microchem. J.* 198, 110175.
- Abou-Melha, K.S., Al-Hazmi, G.A.A., Habeebullah, T.M., Althagafi, I., Othman, A., El-Metwaly, N.M., Shaaban, F., Shahat, A., 2021. Functionalized silica nanotubes with azo-chromophore for enhanced Pd²⁺ and Co⁺ ions monitoring in E-wastes. *J. Mol. Liq.* 329, 115585.
- Al-Hazmi, G.H., Refat, M.S., Shahat, A., 2022. Adsorption of organic dye onto mesoporous aluminosilica monoliths: Equilibrium, kinetic and thermodynamic studies. *ChemistrySelect* 7 (30), e202201995.
- Ali, M.E.A., Atta, A.H., Medhat, M., Shahat, A., Mohamed, S.K., 2021. Effective removal of Methyl blue and Crystal Violet dyes using improved polysulfone/ZIF-8 nanocomposite ultrafiltration membrane. *Biointerface Res. Appl. Chem.* 12, 7942–7956.
- Ambrose, M.A., Dreuw, A., Jensen, F., 2021. Probing basis set requirements for calculating core ionization and core excitation spectra using correlated wave function methods. *J. Chem. Theory Comput.* 17 (5), 2832–2842.
- Awual, M. R., Hasan, M. M., & Shahat, A. (2017). Erratum to: "Functionalized novel mesoporous adsorbent for selective lead (II) ions monitoring and removal from wastewater" [*Sens. Actuators B Chem.* 203 (2014) 854–863]. *Sensors and Actuators B: Chemical*, 100(242), 777.
- Basha, M.T., Shahat, A., Yakout, A.A., 2024. Tailoring the structure of Fe-based NH₂-MIL-88 via 2-hydroxyacetophenone for arsenic removal from aqueous solutions: Kinetics, adsorption isotherms studies, and optimization through Box-Behnken design. *Sens. Actuators, A: Phys.* 373, 115398.
- Besley, N.A., 2021. Modeling of the spectroscopy of core electrons with density functional theory. *Wiley Interdiscip. Rev.: Comput. Mol. Sci.* 11 (6), e1527.
- Bose-O'Reilly, S.; McCarty, K. M.; Steckling, N.; Lettmeier, B.; Mercury Exposure and Children's Health, *Curr Probl Pediatr Adolesc Health Care.* 2010, 186–215.
- Brent, R.N., Wines, H., Luther, J., Irving, N., Collins, J., Drake, B.L., 2017. Validation of handheld X-ray fluorescence for in situ measurement of mercury in soils. *J. Environ. Chem. Eng.* 5 (1), 768–776.
- Brühwiler, D., 2010. Postsynthetic functionalization of mesoporous silica. *Nanoscale* 2, 887–892.
- Chen, K., She, S., Zhang, J., et al., 2015. Label-free colorimetric detection of mercury via Hg₂⁺ ions-accelerated structural transformation of nanoscale metal-oxo clusters. *Sci. Rep.* 5, 16316.
- Chung, T.-H., Wu, S.-H., Yao, M., Lu, C.-W., Lin, Y.-S., Hung, Y., Mou, C.-Y., Chen, Y.-C., Huang, D.-M., 2007. The effect of surface charge on the uptake and biological function of mesoporous silica nanoparticles in 3T3-L1 cells and human mesenchymal stem cells. *Biomaterials* 28, 2959–2966.
- Clarkson, T.W., Magos, L., Myers, G.J., 2003. The toxicology of mercury—current exposures and clinical manifestations. *N. Engl. J. Med.* 349, 1731–1737. <https://doi.org/10.1056/NEJMra022471>.
- Ding, K.L., Hu, B.J., Xie, Y., An, G.M., Tao, R.T., Zhang, H.Y., Liu, Z.M., 2009. A simple route to coat mesoporous SiO₂ layer on carbon nanotubes. *J. Mater. Chem.* 19, 3725–3731.
- Du, X.J., Chen, Y., Qin, L.Y., Luo, H.Q., Li, N.B., Li, B.L., 2021. Plasmonic gold nanoparticles stain hydrogels for the portable and high-throughput monitoring of mercury ions. *Environ. Sci. Tech.* 56 (2), 1041–1052.
- El-Sewify, I.M., Radwan, A., Elghazawy, N.H., Fritzsche, W., Azzazy, H.M., 2022. Optical chemosensors for environmental monitoring of toxic metals related to Alzheimer's disease. *RSC Adv.* 12 (50), 32744–32755.
- El-Sewify, I.M., Radwan, A., Shahat, A., El-Shahat, M.F., Khalil, M.M., 2022. Superior adsorption and removal of aquaculture and bio-staining dye from industrial wastewater using microporous nanocubic Zn-MOFs. *Micropor. Mesopor. Mater.* 329, 111506.
- El-Sewify, I.M., Radwan, A., Azzazy, H.M.E.S., 2023. Multi-responsive paper chemosensors based on mesoporous silica nanospheres for quantitative sensing of heavy metals in water. *RSC Adv.* 13 (10), 6433–6441.
- El-Sewify, I.M., Shenashen, M.A., ElAgamy, R.F., Emran, M.Y., Selim, M.S., Khairy, M., El-Safy, S.A., 2024. Fluorescent sensor/tracker for biocompatible and real-time monitoring of ultra-trace arsenic toxicants in living cells. *J. Hazard. Mater.*, 135429
- Fouda, A.E., Besley, N.A., 2018. Assessment of basis sets for density functional theory-based calculations of core-electron spectroscopies. *Theor. Chem. Acc.* 137 (1), 6.
- Fu, X.C., Chen, X., Guo, Z., Xie, C.G., Kong, L.T., Liu, J.H., Huang, X.J., 2011. Stripping voltammetric detection of mercury (II) based on a surface ion imprinting strategy in electropolymerized microporous poly(2-mercaptobenzothiazole) films modified glassy carbon electrode. *Anal. Chim. Acta.* 685, 21–28.
- Gao, Y., De Galan, S., De Brauwere, A., Baeyens, W., Leermakers, M., 2010. Mercury speciation in hair by headspace injection–gas chromatography–atomic fluorescence spectrometry (methylmercury) and combustion-atomic absorption spectrometry (total Hg). *Talanta* 82, 1919–1923.
- C. Gao, Q. Zhang, Z. Lu, Y. Yin, Templated synthesis of metal nanorods in silica nanotubes, *J. Am. Chem. Soc.* 133 (2011) 19706e19709.
- Grandjean, P., Weihe, P., White, R.F., Debes, F., 1998. Cognitive performance of children prenatally exposed to "Safe" levels of methylmercury. *Environ. Res.* 77, 165–172.
- Harada, M., 1995. Minamata disease: methylmercury poisoning in Jaorganic chromophore caused by environmental pollution. *Crit. Rev. Toxicol.* 25, 1–24.
- Hasan, M.M., 2014. A novel fine-tuning mesoporous adsorbent for simultaneous lead(II) detection and removal from wastewater. *Sens. Actuators, B* 202, 395–403.
- Hasan, M.M., Ihara, T., Yaita, T., 2014. Mesoporous silica based novel conjugate adsorbent for efficient selenium(IV) detection and removal from water. *Micropor. Mesopor. Mater.* 197, 331–338.
- Hasan, M.M., Znad, H., 2015. Organic-inorganic based nano-conjugate adsorbent for selective palladium(II) detection, separation and recovery. *Chem. Eng. J.* 259, 611–619.
- Hassan, H.M.A., Shahat, A., Azzazy, H.M., Abd El-aal, R.M., El-Sayed, W.N., Elwahed, A., Awual, M.R., 2020. A novel and potential chemical sensor for effective monitoring of Fe(II) ion in corrosion systems of water samples. *Microchem. J.* 154, 104578.
- Hosni, M., Abd El-aal, R.M., Shahat, A., El-Sewify, I.M., 2024. Novel multi-function chromoionophoric probe-based nano-conjugate material for highly efficient detection, removal, and recovery of Pd (II) and Co (II) ions from electronic wastes and electroplating wastewater. *ChemistrySelect* 9 (28), e202400557.
- Hudson, S.P., Padera, R.F., Langer, R., Kohane, D.S., 2008. The biocompatibility of mesoporous silicates. *Biomaterials* 29, 4045–4055.
- Hylander, L.D., Goodsite, M.E., 2006. Environmental costs of mercury pollution. *Sci. Total Environ.* 368, 352–370. <https://doi.org/10.1016/j.scitotenv.2005.11.029>.
- Ioannou-Tfofa, L., Raj, S., Prakash, H., Fatta-Kassinos, D., 2019. Solar photo-Fenton oxidation for the removal of ampicillin, total cultivable and resistant E. coli and ecotoxicity from secondary-treated waste-water effluents. *Chem. Eng. J.* 355, 91–102.
- Kamel, R., Shahat, A., Anwar, Z., El-Qady, H., Kilany, E., 2020. Efficient dual sensor of alternate nanomaterials for sensitive and rapid monitoring of ultra-trace phenols in sea water. *J. Mol. Liq.* 297, 111798.
- Khalique, M.A., Ratna, Y., Znad, H., 2015. Simultaneous ultra-trace palladium(II) detection and recovery from wastewater using new class meso-adsorbent. *J. Ind. Eng. Chem.* 21, 405–413.
- Khalil, M.A., El-marghany, A., Kubra, K.T., Shahat, A., 2024. A ratiometric and selective fluorescent nanosensor for determining Hg₂⁺ ions based on a novel functionalized metal-organic framework. *Appl. Organomet. Chem.* 38 (8), e7571.
- Khalil, M.M., Shahat, A., Radwan, A., El-Shahat, M.F., 2016. Colorimetric determination of Cu (II) ions in biological samples using metal-organic framework as scaffold. *Sens. Actuators B: Chem.* 233, 272–280.
- Leermakers, M., Baeyens, W., Quevauviller, P., Horvat, M., 2005. Mercury in environmental samples: Speciation, artifacts and validation. *TrAC Tren. in Anal. Chem.* 24, 383–393.
- Marczenko, Z., & Balcerzak, M. (2000). Separation, preconcentration and spectrophotometry in inorganic analysis (Vol. 10). Elsevier.
- Mazroua, A.M., Mansour, A.A., Abed, M.Y., Youssif, M.A., Shenashen, M.A., Awual, M. R., 2019. Nano-composite multi-wall carbon nanotubes using poly(pphenylene terephthalamide) for enhanced electric conductivity. *J. Environ. Chem. Eng.* 7, 103002.
- M.J.S. McGrath, C.N. Scanaill, Sensing and sensor fundamentals, in: *Sensor Technologies: Healthcare, Wellness and Environmental Applications*, Apress, New York, 2013, pp. 15e50.
- Mercury Update: Impact on Fish Advisories, EPA Off. Water Merc. Updat. Impact Fish Advis. EPA Fact Sheet EPA-823-F-01-011, Washing. DC. 2001.
- Mohamed, S.K., Shahat, A., Atito, M., Kamel, R.M., 2024. Efficient and low-cost mesoporous magnetic carbon composites derived from date palm stones for environmental remediation of hexavalent chromium. *J. Porous Mater.* 1–15.
- Moreno, F., Garcia-Barrera, T., Gomez-Ariza, J.L., 2010. Simultaneous analysis of mercury and selenium species including chiral forms of selenomethionine in human urine and serum by HPLC column-switching coupled to ICP-MS. *Analyst* 135, 2700–2705.
- Natale, F.D., Lancia, A., Molino, A., Natale, M.D., Karatza, D., Musmarra, D., 2006. Capture of mercury ions by natural and industrial materials. *J. Hazard. Mater.* 132, 220.
- Pan, Y., Zhang, Y., Zhou, M., Cai, J., Li, X., Tian, Y., 2018. Synergistic degradation of antibiotic sulfamethazine by novel pre-magnetized Fe₀/PS process enhanced by ultrasound. *Chem. Eng. J.* 354, 777–789.
- Pulicharla, R., Hegde, K., Brar, S.K., Surampalli, R.Y., 2017. Tetracyclines metal complexation: Significance and fate of mutual existence in the environment. *Environ. Pollut., Ser. B* 221, 1–14.
- Radwan, A., El-Sewify, I.M., Shahat, A., Azzazy, H.M., Khalil, M.M., El-Shahat, M.F., 2020. Multiuse Al-MOF chemosensors for visual detection and removal of mercury ions in water and skin-whitening cosmetics. *ACS Sustain. Chem. Eng.* 8 (40), 15097–15107.
- Radwan, A., El-Sewify, I.M., Shahat, A., El-Shahat, M.F., Khalil, M.M.H., 2020. Decorated nanosphere mesoporous silica chemosensors for rapid screening and removal of toxic cadmium ions in well water samples. *Microchem. J.* 156, 104806.
- Radwan, A., El-Sewify, I.M., Azzazy, H.M.E.S., 2022. Monitoring of cobalt and cadmium in daily cosmetics using powder and paper optical chemosensors. *ACS Omega* 7 (18), 15739–15750.
- Rizk, M.A., Yahya, R., Alsaiari, R.A., Alsaiari, M.A., Shahat, A., Elshaarawy, R.F., 2024. Carboxymethyl-imidazolium O-vanillin Schiff base grafted into NH₂-tagged MIL-101

- (Cr) for effective removal of cupric ions from aqueous effluents. *Environ. Sci. Pollut. Res.* 1–16.
- Sarang, R., Vidal, M.L., Coriani, S., Krylov, A.I., 2020. On the basis set selection for calculations of core-level states: Different strategies to balance cost and accuracy. *Mol. Phys.* 118 (19–20), e1769872.
- Shahat, A., Mohamed, M.H., Awual, R., Mohamed, S.K., 2020. Novel and potential chemical sensors for Au(III) ion detection and recovery in electric waste samples. *Microchem. J.* 158, 105312.
- Shahat, A., Alosaimi, A.M., Hussein, M.A., El-Said, W.A., 2022. Azo-chromophore based on functionalized silica nanotubes for enhanced identification of Pd (II) ions in e-residues. *J. Mater. Res. Technol.* 17, 2550–2559.
- A. Shahat, E.A. Ali Mohammad, M.F. El Shahat, Colorimetric determination of some toxic metal ions in post-mortem biological samples, *Sensor. Actuator. B Chem.* 221 (2015) 1027e1034.
- Vila, M., Hueso, J.L., Manzano, M., Izquierdo-Barba, I., de Andres, A., Sanchez-Marcos, J., Prieto, C., Vallet-Regi, M., 2009. Carbon nanotubes-mesoporous silica composites as controllable biomaterials. *J. Mater. Chem.* 19, 7745–7752.
- Wang, B., Lv, X.-L., Feng, D., Xie, L.-H., Zhang, J., Li, M., Xie, Y., Li, J.-R., Zhou, H.-C., 2016. Highly stable Zr (IV)-based metal–organic frameworks for the detection and removal of antibiotics and organic explosives in water. *J. Am. Chem. Soc.* 138, 6204–6216.
- Wang, Y., Yang, F., Yang, X., 2010. Colorimetric biosensing of mercury (II) ion using unmodified gold nanoparticle probes and thrombin-binding aptamer. *Biosens. Bioelectron.* 25, 1994–1998.
- X.F. Yang, H. Tang, K.S. Cao, H.J. Song, W.C. Sheng, Q. Wu, Templated-assisted one-dimensional silica nanotubes: synthesis and applications, *J. Mater. Chem.* 21 (2011) 6122e6135.
- Yang, J., Lee, J.Y., Ying, J.Y., 2011. Phase transfer and its applications in nanotechnology. *Chem. Soc. Rev.* 40, 1672–1696.
- You, L., Zha, D., Anslyn, E.V., 2015. Recent advances in supramolecular analytical chemistry using optical sensing. *Chem. Rev.* 115, 7840–7892.
- Zahir, F., Rizwi, S.J., Haq, S.K., Khan, R.H., 2005. Low dose mercury toxicity and human health. *Environ. Toxicol. Pharmacol.* 20, 351–360. <https://doi.org/10.1016/j.etap.2005.03.007>.
- Zhang, H., Luo, J.J., Sun, Z., Zou, H.L., Luo, H.Q., Li, N.B., Li, B.L., 2022. Hydrogels allow the precise growth tracking of plasmonic gold nanoparticles for mercury analysis. *J. Mater. Chem. C* 10 (39), 14508–14516.
- Zhao, D., Wan, Y., 2007. On the controllable softtemplating approach to mesoporous silicates. *Chem. Rev.* 107, 2821–2860.
- Zheng, N., Wang, Q., Zhang, X., Zheng, D., Zhang, Z., Zhang, S., 2007. Population health risk due to dietary intake of heavy metals in the industrial area of Huludao City, China. *Sci. Total Environ.* 387, 96–104.
- Zhu, L.R., Wang, Z.Y., Luo, J.J., Zheng, Y.J., Zou, H.L., Luo, H.Q., Li, B.L., 2023. Mercury-mediated epitaxial accumulation of Au atoms for stained hydrogel-improved on-site mercury monitoring. *Anal. Chem.* 95 (51), 18859–18870.